Study on IEEE 2800-2022 Standard Benefits for Transmission Line Protection in the Presence of Inverter-Based Resources

Moisés J. B. B. Davi, Mário Oleskovicz, Felipe V. Lopes

Abstract—This paper presents an Electromagnetic Transient (EMT)-based study about the IEEE 2800-2022 standard benefits for transmission line protection functionalities in the presence of Inverter-Based Resources (IBR). Seven functions are evaluated, namely: 1) Self-polarized distance protection, 2) Memory-polarized distance protection, 3) Memory-Cross-polarized distance protection, 4) Negative sequence-based directional function, 5) Zero sequence-based directional function, 6) Incremental phasor-based phase-selection function, and 7) Current angle-based phase-selection function. To do so, massive EMT simulations are carried out in the PSCAD environment to emulate contingency scenarios in a typical transmission circuit that interconnects an IBR to a synchronous power grid. The evaluated protection functions are implemented and validated with the routines applied in commercial relays, providing a practical perspective on the importance of recent advances in IBR control standards, such as the IEEE 2800-2022. The results demonstrate that the IEEE 2800-2022 significantly improves the transmission line protection performance, being the EMT-based analysis crucial to provide a detailed study on these benefits.

Keywords—Directional Protection, Distance Protection, IEEE 2800-2022, Inverter-Based Generators, Phase-Selection Functions, Renewable Energy.

I. INTRODUCTION

THE increasing penetration of Inverter-Based Resources (IBRs) in modern power grids and the use of different Fault Ride Through strategies [1] have resulted in atypical fault contributions in electrical systems interconnecting IBRs. Hence, the assessment of IBR impacts on protection schemes has been widely studied worldwide [2]–[13].

Among the challenges experienced by protection schemes in the presence of IBRs, problems in non-unit protections stand out [2]. Indeed, differential protection available in commercial relays has proved to be dependable [3], but the traditional distance protection is prone to malfunction [2], [3], which is a cause of concern if communication channels are lost. Thus, various studies about IBR impacts on distance protection have been conducted, mainly because most large inverter-based renewable power plants are connected to the grid through sub-transmission and transmission lines (TLs).

Most studies available in the open literature evaluate only whether distance protection operates or not [3], [4]. Some works address the apparent impedance trajectories calculated by distance protection elements in the presence of IBRs, highlighting the challenges that can take place during faults [2], [5], [10]–[13]. However, the influence of different IBR grid codes on protection performance is commonly disregarded. Even when more profound studies on grid codes are carried out, comprehensive investigations on the main fault types and characteristics are not presented. In addition, from the authors' best knowledge, works explaining the influence of negative sequence current generation following the recently published IEEE 2800-2022 standard [14] on distance protection have not yet been reported.

Other literature gaps can be identified when the impact of IBRs on directional and phase-selection functions is considered [6]–[9]. Most works either focus on directional functions only [6], [7] or the phase-selection methods [8], [9].

Aiming to fill the abovementioned literature gaps, this paper presents an EMT-based study that explains how the IEEE 2800-2022 standard influences the operation of IBRs and, consequently, the protection performance. Full-Converter Wind Generators (FCWG) are simulated to assess seven protection functions often applied in commercial relays, namely: 1) Self-polarized distance protection, 2) Memory-polarized distance protection, 3) Memory-Cross-polarized distance protection, 4) Negative sequence-based directional function, 5) Zero sequence-based directional function, 6) Incremental phasor-based phase-selection function, and 7) Current angle-based phase-selection function. In summary, the paper intends to answer the question: "How do advances in standardizations of IBR controls, such as IEEE 2800-2022 [14], favor the operation of conventional protection functions?".

Several EMT simulations are carried out in the PSCAD environment to emulate fault scenarios in a transmission system that interconnects IBRs to a synchronous power grid. The impacts of outdated and recent grid codes for IBR controls on protection functions are compared, both by simulations and by tests on a commercial relay, proving the mitigation of problems when recent standardized requirements are considered. Moreover, technical explanations are provided for such improvements, highlighting the benefits of the new grid code requirements.

II. Advances in Standards for Inverter-Based Resource Controls

Among the IBR operational features that can affect conventional protection functions, the low fault contribution levels and the diversity of inverter control strategies stand out [15]. The fault current limitation (typically not exceeding 1.2 p.u. [15]) is justified by the thermal restrictions of the inverters. Thus, since it is necessary to safeguard the inverter elements, modifications in such a feature are commonly not considered in the control context. On the other hand, inverter control methodologies have evolved over the years, such that several studies have focused on solutions to minimize the impacts of IBRs on existing protections.

This paper considers two control groups (shown in Fig. 1) to highlight the implications of IBR control advances:

- **Group 1 Controls (G1C)**: represent the first strategies that emerged, based only on positive sequence components, also called Coupled Sequence Controls [16]. The most striking feature of such a control group is the suppression of negative sequence currents, even for asymmetrical disturbances. Moreover, in this control type, active and reactive power are regulated based on simple voltage controllers at the DC link and the coupling point, respectively [17].
- **Group 2 Controls (G2C)**: represent the most recent strategies, compliant with IEEE 2800-2022 [14], injecting additional levels of reactive current after the fault detection, being such injection dictated by the voltage variation measured at the IBR coupling point [18]. In this strategy, negative sequence currents are also provided, injected with levels proportional to the measured negative sequence voltages, and leading such voltages by a phase angle between 90 and 100 degrees [14]. To do so, another control scheme known as Decoupled Sequence Control is used [16]. Besides providing reactive support to the grid under disturbance conditions, the new grid codes aim to make the IBR positive and negative sequence

impedances (during faults) more similar to those of conventional synchronous generators. These principles have been considered for protection design purposes since the early stages of electrical power systems.

Fig. 1 illustrates a schematic of G1C and G2C, with G2C innovations [14] highlighted in red.

III. Test System for the Studies

The influence of grid codes on the behavior of IBRs during faults can be verified in both steady-state and transient conditions. In this sense, several important aspects of IBR responses cannot be analyzed through classical phasor-domain fault simulations, so the use of EMT for detailed protection studies in the presence of IBRs has been considered essential [19]. With that, the PSCAD platform is used in this paper to model the test system shown in Fig. 2. Table I shows the test system parameters.

In this context, the modeling of FCWGs for the studies in this paper is in line with the topologies already widely reported and consolidated in the literature [20], [21]. The inverter controls were adjusted as described in [22], with adaptations based on [14], [16] to ensure compliance with the requirements of the IEEE 2800-2022 standard (see Fig. 1). The DC link consists of a 0.015 Farad capacitor with a nominal voltage of 1450 V. The coupling choke circuit has a resistance of 0.003 p.u. and an inductance of 0.15 p.u. at the machine base, and the RC output filter has a power of 120 kvar. The Chopper circuit was designed to operate when the DC link voltage exceeds 1.15 p.u.. It is disabled when this voltage reaches values below 1.05 p.u.. The nominal data for the permanent magnet synchronous generators are: $S_n = 1.5$ MVA; $V_n = 690$ V; $R_s = 0.0017$ p.u.; $X_l = 0.0364$ p.u.; $X_d = 0.55$ p.u.; $R_{kd} = 0.055$ p.u.; $X_{kd} = 0.62$ p.u.; $X_q = 1.11$ p.u.; $R_{kq} = 0.183$ p.u.; $X_{kq} = 1.175$ p.u..
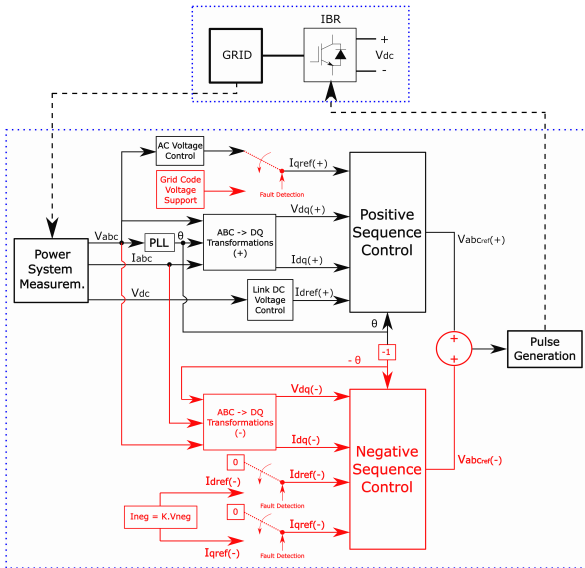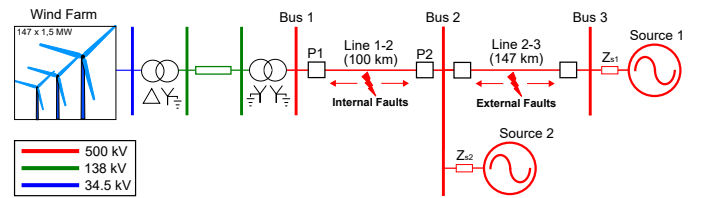

Fig. 2. Test system single-line diagram.

TABLE I
TEST SYSTEM PARAMETERS.

Parameters	Values
Source 1	$V_{s1} = 490.196 \angle 0°$ kV R+/0 = 3.941 / 13.878 Ω L+/0 = 114.901 / 229.827 mH
Source 2	$V_{s2} = 480.392 \angle 15°$ kV R+/0 = 4.970 / 1.008 Ω L+/0 = 1079.09 / 255.47 mH
Transformer Dyn11 (34.5 – 0.575 kV)	1.75 MVA – Z = 6%
Transformer YNd1 (138 - 34.5 kV)	90 MVA – Z = 10%
Transformer YNyn0 (500 – 138 kV)	250 MVA – Z = 10%
Lines 1-2 and 2-3	R+/0 = 0.017 / 0.331 Ω/km L+/0 = 0.839 / 2.382 mH/km C+/0 = 0.0137 / 0.0082 μF/km

Fig. 1. Schematic of the considered inverter control methodologies (G2C innovations highlighted in red).

In the test system, the active and reactive powers supplied by the FCWG to the grid are controlled at 220.5 MW and 0 var, respectively. For the sake of comparison, G1C and G2C are considered during the studied EMT simulations.

In the proposed investigations, short-circuits on both lines 1-2 and 2-3 are simulated, varying the type (AG, BG, CG, AB, BC, CA, ABG, BCG, CAG, and ABC), fault resistance between phases (R_{ph} equal to 0, 1, 1.5, and 2.5 Ω) and to the ground (R_g equal to 0, 25, 50, and 100 Ω), inception angle (0° and 90°), and fault location (faults on Line 1-2, from 0% to 100% with steps of 10%, being 0% the point P1, and on Line 2-3 at 5% and 50%, being 0% the bus 2). Thus, considering the different FCWG controls, 8320 scenarios are evaluated.

In all simulations, currents and voltages are obtained from current and potential transformers installed at points P1 and P2 (see Fig. 2), whose transformation ratios are 60 and 4500, respectively. The signals are processed by 3rd order anti-aliasing filters with a cutoff frequency of 180 Hz. Further details on the protections are provided in the next sections.

IV. Influence of IEEE 2800-2022 on Directional and Phase-Selection Functions

In this section, the EMT simulations are used to quantify the number of operations of 1) Negative sequence-based and 2) Zero sequence-based directional functions, 3) Incremental phasor-based, and 4) Current angle-based phase-selection functions. The decision-making procedures are carried out from quantities measured 100 ms after the fault inception, encompassing the response time of the FCWG controls, typically on the order of 50 ms [14]. Furthermore, to facilitate the analysis of contributions that come from conventional generation (at P2) and IBRs (at P1), only faults on Line 1-2 (a total of 7040 scenarios) are evaluated in the section.

A. Negative Sequence-Based Directional Function

1) Function Modeling Considerations [23], [24]: In the assessed algorithm, a scalar value Z_2 is calculated [23]:

$$Z_2 = \frac{Re[\overrightarrow{V_2} \cdot (1\angle\theta_{L1} \cdot \overrightarrow{I_2})^*]}{|\overrightarrow{I_2}|^2} \ , \tag{1}$$

being $\overrightarrow{V_2}$ and $\overrightarrow{I_2}$ are the negative-sequence voltage and current phasors, respectively, and θ_{L1} is the TL positive-sequence impedance angle. This directional element declares a forward fault when the value of Z_2 is smaller than a direct threshold (Z2F), which is typically set as half the positive sequence impedance of the protected TL. On the other hand, a reverse fault is declared when Z_2 presents values higher than a reverse threshold (Z2R), typically set as Z2F plus an impedance of 0.2 Ω [23]. There are also some restrictions for the operation of this directional element regarding the negative sequence current levels, i.e., $3|\overrightarrow{I_2}| > 0.25|\overrightarrow{I}_{nominal}|$ according to [24]. For the quantitative analysis, the typical thresholds and restrictions are considered.

2) Quantitative Analysis Results: Fig. 3 illustrates the success rates of the evaluated negative sequence impedance-based directional function for Phase-to-Ground (PG), Phase-to-Phase (PP), and Phase-to-Phase-to-Ground
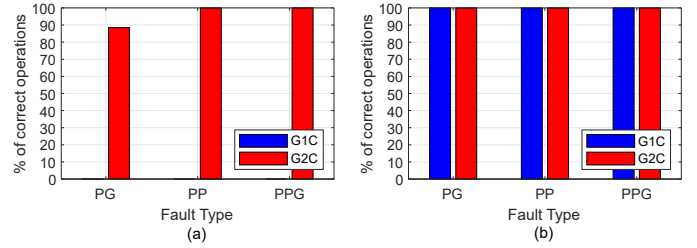

Fig. 3. Negative sequence impedance-based directional function performance by fault type, considering measurements at (a) P1 and (b) P2.

(PPG) fault types. Both G1C and G2C are considered, and measurements from points P1 (wind power plant side) and P2 (grid side) are evaluated.

It is noticed that the suppression of negative sequence currents (as occurs for G1C) results in reliability problems on the directional function applied at point P1 (IBR side). Indeed, in all analyzed scenarios, the directional element is blocked at P1 when G1C is used, whereas it properly operates at point P2 (grid side). On the other hand, applying G2C, 100% of correct operations are verified for PP and PPG fault cases and 90% for PG cases. Regarding the PG cases, it is important to clarify that errors were verified only for high fault resistance cases. In these scenarios, the negative sequence voltages are reduced during the fault, leading the control to inject minimal levels of negative-sequence currents.

For the point P2 measurements, regardless of the adopted control, correct operations of the directional function shown in (1) are verified since the current contributions measured at such a terminal originate from conventional generations.

B. Zero Sequence-Based Directional Function

1) Function Modeling Considerations [24]: Basically, a scalar value Z_0 is calculated [24] using:

$$Z_0 = \frac{Re[3\overrightarrow{V_0} \cdot (1\angle\theta_{L0} \cdot 3\overrightarrow{I_0})^*]}{|3\overrightarrow{I_0}|^2} \ , \tag{2}$$

where $\overrightarrow{V_0}$ and $\overrightarrow{I_0}$ are the zero-sequence voltage and current phasors, respectively, and θ_{L0} is the TL zero-sequence impedance angle. This directional element operates analogously to the presented negative-sequence element. It declares a forward fault when the value of Z_0 is smaller than a direct threshold (Z0F), typically set as half the zero-sequence impedance of the protected TL. On the other hand, a reverse fault is declared when Z_0 reaches levels higher than a reverse threshold (Z0R), which is, in turn, typically set as Z0F plus an impedance of 0.2 Ω [24]. Similarly to the negative-sequence element, there are also restrictions to apply for zero-sequence directional protection, which regard the zero sequence current levels, i.e., $3\overrightarrow{I_0} > 0.5\overrightarrow{I}_{nominal}$ according to [24]. For the quantitative analysis, the typical thresholds and restrictions are applied.

2) Quantitative Analysis Results: Fig. 4 depicts the zero sequence impedance-based directional function percentages of correct operations for PG and PPG faults. G1C and G2C are considered, evaluating measurements from points P1 and P2.

The results show that regardless of the FCWG control type and considered measurement point, the zero-sequence
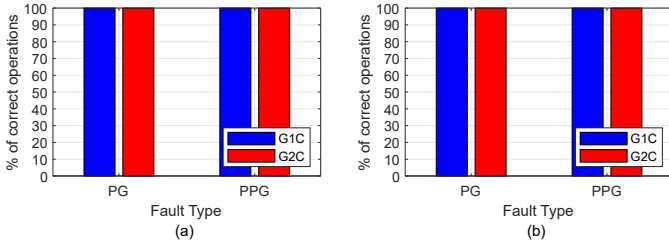
Fig. 4. Zero sequence impedance-based directional function performance by fault type, considering measurements at (a) P1 and (b) P2.
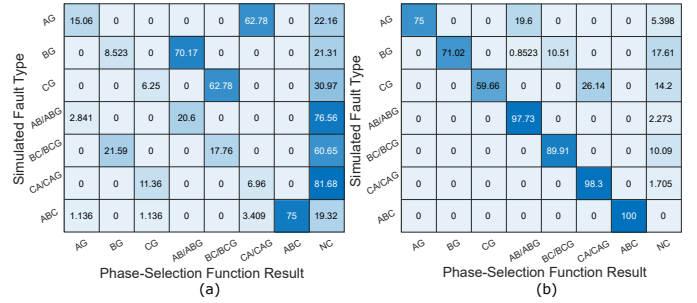

Fig. 5. Incremental phasors-based phase-selection function performance, by fault type, for measurements at P1, and considering (a) G1C and (b) G2C.

impedance-based directional function satisfactorily operated for all faults involving the ground. It occurs because high zero sequence contributions are verified at both P1 and P2 points, being independent of the wind power plant generation characteristics. Indeed, the zero sequence contributions measured at point P1 originate from the grid (not from the IBR), returning through the grounded neutral point of YNyn0 transformer.

C. Incremental Phasor-Based Phase-Selection Function

1) Function Modeling Considerations [25], [26]: The algorithm is based on the calculation of three incremental torques [25], which are given by:

$$\Delta T_{ab} = Re[\overrightarrow{\Delta V_{ab}} \cdot (1\angle\theta_{L1} \cdot \overrightarrow{\Delta I_{ab}})^*] , \quad (3)$$

$$\Delta T_{bc} = Re[\overrightarrow{\Delta V_{bc}} \cdot (1\angle\theta_{L1} \cdot \overrightarrow{\Delta I_{bc}})^*] , \quad (4)$$

$$\Delta T_{ca} = Re[\overrightarrow{\Delta V_{ca}} \cdot (1\angle\theta_{L1} \cdot \overrightarrow{\Delta I_{ca}})^*] , \quad (5)$$

where $\overrightarrow{\Delta V_{ab}}$, $\overrightarrow{\Delta V_{bc}}$ and $\overrightarrow{\Delta V_{ca}}$ are incremental voltage phasors, $\overrightarrow{\Delta I_{ab}}$, $\overrightarrow{\Delta I_{bc}}$ and $\overrightarrow{\Delta I_{ca}}$ are incremental current phasors, and θ_{L1} is the TL positive sequence impedance angle. The incremental voltage and current phasors are usually obtained by subtracting the fault quantities from the pre-fault ones [26].

For the faulty phase selection, the relations shown in Table II are assumed for the proposed quantitative study [25]. For each fault type, ΔT_{ab}, ΔT_{bc}, and ΔT_{ca} are normalized by the maximum value between them and compared to the parameters L_{up}, L_{int}, and L_{low}, representing the algorithm sensitivity thresholds. Here, $L_{up} = 0.7$, $L_{int} = 0.5$, and $L_{low} = 0.35$ are used. Finally, scenarios that do not meet any of the relations shown in Table II are classified as "Not Classified" (NC).

2) Quantitative Analysis Results: Firstly, it is worth mentioning that, at point P2 (see Fig. 2), regardless of the FCWG control, the phase selection was satisfactory for 100% of the evaluated scenarios. Indeed, at this terminal, the measured current contributions originate from conventional generations, and this phase-selection function was originally

designed considering the characteristics of these generators. Thus, the results at this terminal are not detailed. On the other hand, considering measurements from point P1, phase-selection issues take place, being the percentages of correct operations illustrated in Figs. 5-a and 5-b for control groups G1C and G2C, respectively.

As shown in Fig. 5-a, for G1C, the higher percentage of correct answers (75%) was obtained for three-phase faults, in which only positive sequence components are generated. As a result, the G1C presents satisfactory results. However, for single-phase faults, it can be seen that about 65% are classified as PP/PPG faults and 25% as NC. For two-phase faults, about 73% are classified as three-phase. The suppression of negative sequence components mainly justifies the low percentage of correct phase selections when considering the G1C.

Analyzing Fig. 5-b, which regards the G2C, the benefits of advances in IBR grid codes become evident since the average percentage of correct operations for single-phase and two-phase faults increased from 9.94% and 15.1% (considering G1C) to 68.56% and 95.31% (considering G2C), respectively. Even for three-phase faults, an improvement was noticed, as the percentage of correct operations was increased from 75% to 100%. Therefore, G2C led the incremental phasor-based phase-selection function to perform better since the positive and negative sequence impedances of FCWG during faults tend to present characteristics closer to those of conventional generators.

D. Current Angle-Based Phase-Selection Function

1) Function Modeling Considerations [27], [28]: The main current angle-based phase-selection functions have their operation defined, as depicted in Fig. 6. When the angular difference between the negative and zero sequence currents is in the regions of Fig. 6-a, the decision for the PG or PPG fault types is made based on the lowest mho element (PG or PP) calculated reach [27], [28]. On the other hand, for the cases where the angular difference is in the regions of Fig. 6-b, the decision-making is based on the calculations of the PG and PP distance element resistances, selecting the one with the lowest resistance estimation [27], [28].

In addition, in [28], checking the levels of negative and zero sequence currents is recommended before analyzing the phase angle information for decision-making. Thus, in this paper, aiming to guarantee a realistic and reliable implementation of the current angle-based phase-selection function, the same
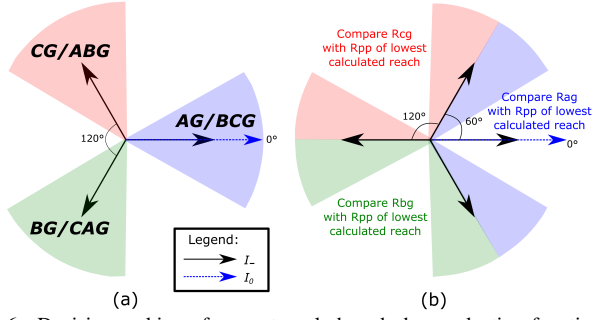
TABLE II
PHASE-SELECTION METHODOLOGY.

Fault Type	ΔT_{ab}	ΔT_{bc}	ΔT_{ca}
AG	$> L_{up}$	$< L_{low}$	$> L_{up}$
BG	$> L_{up}$	$> L_{up}$	$< L_{low}$
CG	$< L_{low}$	$> L_{up}$	$> L_{up}$
AB / ABG	$> L_{up}$	$< L_{int}$	$< L_{int}$
BC / BCG	$< L_{int}$	$> L_{up}$	$< L_{int}$
CA / CAG	$< L_{int}$	$< L_{int}$	$> L_{up}$
ABC	$> L_{up}$	$> L_{up}$	$> L_{up}$

Fig. 6. Decision-making of current angle-based phase-selection functions.

Fig. 7. Current angle-based phase-selection function performance, by fault type, for measurements at P1, and considering (a) G1C and (b) G2C.

thresholds applied to the directional functions based on the negative and zero sequence impedances are considered [24].

2) Quantitative Analysis Results: Starting with the results, Fig. 7 illustrates the percentages of correct operations for all fault types, with measurements at P1, considering G1C (Fig. 7-a) and G2C (Fig. 7-b).

By analyzing the results of Fig. 7, it is observed that the suppression of the negative sequence current when G1C has used results in blocking the current angle phase-selection function by the current level restriction $3\overrightarrow{I_2} > 0.25 \overrightarrow{I}_{nominal}$. However, considering G2C, average success rates of 88.44% and 81.34% for single-phase and two-phase faults were obtained, respectively, proving the positive impacts of recent advances in the standardization of IBRs controls in the context of phase selection procedures.

Finally, it is important to point out that, again, for the measurements taken from point P2, a success rate of 100% was obtained because current contributions are from the grid. Hence, no issues are verified in the phase-selection algorithm, irrespective of the used FCWG control type.

V. INFLUENCE OF IEEE 2800-2022 ON DISTANCE PROTECTION

This section performs a quantitative analysis of the operation of self-polarized, memory-polarized, and memory-cross-polarized Mho distance protection functions.

A. Distance Function Modeling Considerations

The operations of distance protection algorithms are based on the calculation of operating ($\overrightarrow{V_{op}}$) and polarizing ($\overrightarrow{V_{pol}}$) quantities, as shown in Table III for the AG and AB loops [29]. The same equations can be adapted for the other fault loops by substituting the faulted phases [29]. In Table III, Z_R is the protection zone impedance reach; $\overrightarrow{I_A}$, $\overrightarrow{I_B}$, and $\overrightarrow{I_0}$ are

the phasors of phase A, phase B, and zero-sequence currents, respectively; $\overrightarrow{V_A}$, $\overrightarrow{V_B}$, and $\overrightarrow{V_C}$ are the voltage phasors; k_0 is the zero-sequence compensation factor, being the subscript _M used to denote the memorized quantities.

The phase comparator theory is applied in this paper. Hence, an angle α (called phase comparator) is calculated as the angular difference between the operation and polarizing quantities. Therefore, the distance protection is programmed to identify a fault in a given protection zone when it's respective α is between $\pm 90°$.

B. Quantitative and Theoretical Studies

For the evaluated distance functions, a protection zone with a reach of 75% of the TL positive sequence impedance is considered. Moreover, an intentional delay of 50 ms is applied to encompass the response time of FCWG controls [14]. Faults on lines 1-2 and 2-3 are evaluated, and operations of distance functions are monitored over a total fault period of 150 ms. The memory filter described in [30] reproduces the memorized voltages. Thus, three possible classifications are defined for the quantitative analyses: 1) Correct Operations: the protection operates for faults within the zone 1 range or not for defects outside zone 1; 2) Incorrect Operations (Missed Trips): scenarios where there is no protection operation for faults within the zone 1; and 3) Incorrect Operations (Undue Trips): scenarios in which there is a protection operation for faults outside zone 1.

The obtained results considering the 8320 scenarios simulated in PSCAD are illustrated in Figs. 8 and 9, for measurements taken at points P2 and P1, respectively.

Considering measurements at P2 (Fig. 8), i.e., at the grid side, in 84.61% of cases, the fault current contributions come from conventional generators (except for Line 2-3 faults). Hence, the reduced percentages of correct operations obtained for single-phase faults are expected, for which higher fault resistances are simulated since the Mho regions have a reduced resistive reach, which varies proportionally with the reactive reach [29]. However, as this paper focuses on the influence of different IBR control groups on protection performance, it is clear that, for single-phase faults, the adopted controls had no

TABLE III
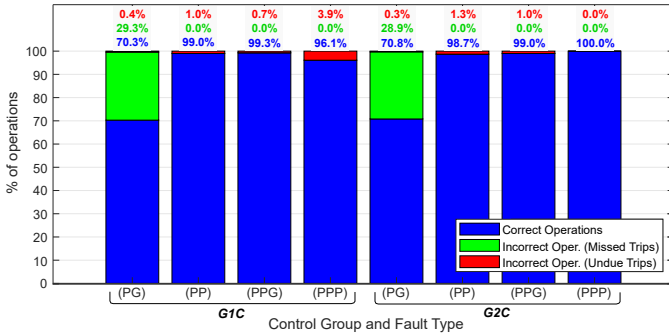OPERATING AND POLARIZING QUANTITIES (AG AND AB FAULT LOOPS).

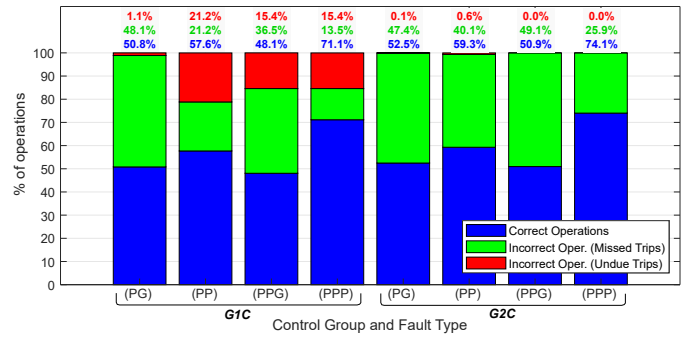| Self-Polarized Distance Function		
Fault Loop	$\overrightarrow{V_{op}}$	$\overrightarrow{V_{pol}}$
AG	$Z_R \cdot (\overrightarrow{I_A} + k_0 \cdot \overrightarrow{I_0}) - \overrightarrow{V_A}$	$\overrightarrow{V_A}$
AB	$Z_R \cdot (\overrightarrow{I_A} - \overrightarrow{I_B}) - (\overrightarrow{V_A} - \overrightarrow{V_B})$	$(\overrightarrow{V_A} - \overrightarrow{V_B})$
Memory-Polarized Distance Function		
Fault Loop	$\overrightarrow{V_{op}}$	$\overrightarrow{V_{pol}}$
AG	$Z_R \cdot (\overrightarrow{I_A} + k_0 \cdot \overrightarrow{I_0}) - \overrightarrow{V_A}$	$\overrightarrow{V_A}\_M$
AB	$Z_R \cdot (\overrightarrow{I_A} - \overrightarrow{I_B}) - (\overrightarrow{V_A} - \overrightarrow{V_B})$	$(\overrightarrow{V_A} - \overrightarrow{V_B})\_M$
Memory-Cross-Polarized Distance Function		
Fault Loop	$\overrightarrow{V_{op}}$	$\overrightarrow{V_{pol}}$
AG	$Z_R \cdot (\overrightarrow{I_A} + k_0 \cdot \overrightarrow{I_0}) - \overrightarrow{V_A}$	$j(\overrightarrow{V_B} - \overrightarrow{V_C})\_M$
AB	$Z_R \cdot (\overrightarrow{I_A} - \overrightarrow{I_B}) - (\overrightarrow{V_A} - \overrightarrow{V_B})$	$-j\overrightarrow{V_C}\_M$
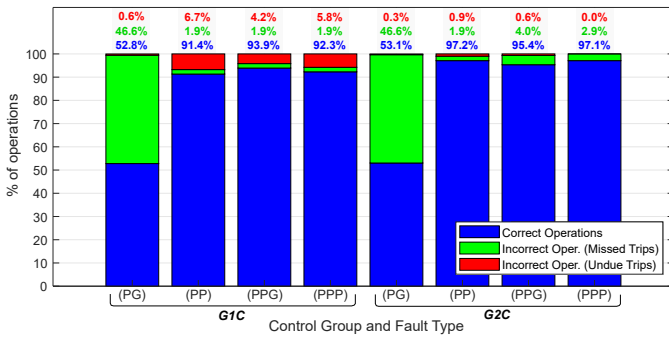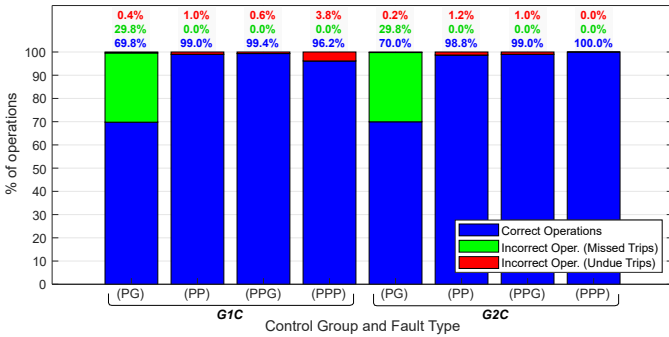
Fig. 8. Operating percentages for (a) self-polarized, (b) memory-polarized, and (c) memory-cross-polarized distance protections, considering both control groups and measurements at P2.

Fig. 9. Operating percentages for (a) self-polarized, (b) memory-polarized, and (c) memory-cross-polarized distance protections, considering both control groups and measurements at P1.

significant impact on the obtained percentages. For two-phase and three-phase faults, in turn, the rate of incorrect operations by undue trips (observed in Line 2-3 fault scenarios) was almost completely eliminated when using G2C. Moreover, it is possible to notice a higher percentage of correct operations for the memory-polarized and memory-cross-polarized functions for all considered fault types and IBR controls.

Analyzing the results obtained for measurements at P1 (Fig. 9), it is noticed that reduced percentages of correct operations occur for single-phase faults, which the use of the Mho characteristic can justify. It is also observed that the adopted IBR controls had no significant influence on the percentages obtained for this fault type. It is valid because zero-sequence-dominated currents occur for PG loops (see Table III). Thus, since zero-sequence currents measured at P1 come from the grid, they have higher magnitudes than IBR phase contributions, such that, for single-phase faults, the IBR controls do not significantly influence the protection.
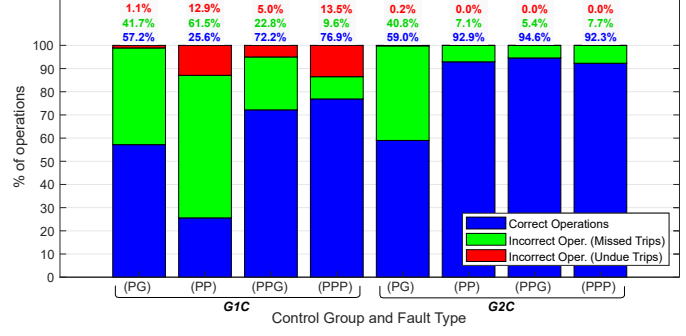
For the other fault types (PP, PPG, and PPP), considering firstly the self-polarized distance protection (Fig. 9-a), the
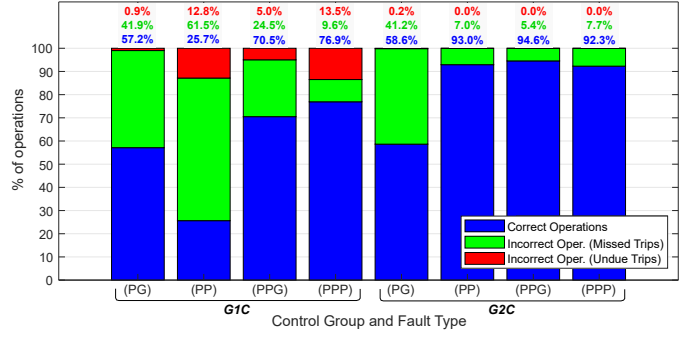
percentages of incorrect operations by undue trips had an average of 17.3% considering the G1C. In contrast, these operation issues were almost completely eliminated when considering the G2C. Thus, besides providing a slight increase in the percentage of correct operations, the adoption of G2C also improved protection security.

Fig. 10 illustrates the impedance trajectories obtained at P1, considering G1C (Fig. 10-a) and G2C (Fig. 10-b) for internal (50% of Line 1-2) and external (on Line 2-3 at 5%, being 0% the bus 2) AB faults, varying the fault resistance. These figures show that different direction trends of the trajectory shift with increasing fault resistance take place, depending on the adopted controls. Using G1C, the Mho element is more susceptible to undue trips. At the same time, it is closer to the expected behavior for systems with conventional generators (rightward shifts) when G2Cs are employed.

The results for two- and three-phase faults measured at point P1 and assuming the memory-polarized distance function (Fig. 9-b) were also evaluated. It can be seen that, besides providing greater operational security (by eliminating incorrect
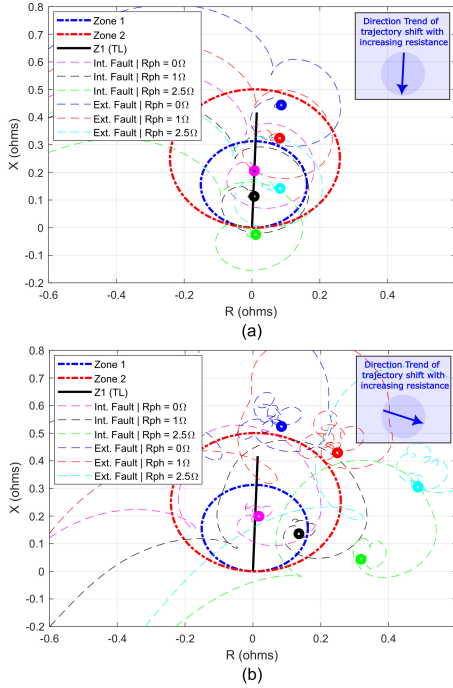
Fig. 10. Impedance trajectories obtained for internal and external AB faults, with fault resistance (R_{ph}) variation and considering (a) G1C and (b) G2C.

Fig. 11. Obtained phase comparators for internal and external AB faults, with fault resistance (R_{ph}) variation and considering (a) G1C and (b) G2C.

operations by undue trips), the use of G2C allowed an increase in correct operations of about 20% of PPG and PPP fault cases, and of about 70% of PP fault scenarios, reaching an average percentage of proper operations of about 93.3%. The conclusions drawn for the memory-polarized function are similar to the memory-cross-polarized distance function.

Fig. 11 shows the phase comparators obtained at P1, with G1C (Fig. 11-a) and G2C (Fig. 11-b), for internal and external AB faults, with fault resistance variation, considering the memory-polarized element. G2C provided greater security and stability to memory-polarized distance functions, especially for faults inside the protected zone (shown in red in Fig. 11).

From the presented results, it is concluded that, in general, G2C allows a safer operation for distance protection, providing efficient support to memory-polarized and memory-cross-polarized distance functions for PP, PPG, and PPP faults. It occurs because the advances in the new standards of IBR controls (such as the IEEE 2800-2022 [14]) focus mainly on emulating conventional synchronous generations regarding the IBR positive and negative sequence impedances under system disturbance conditions, which improves the performance of traditional protection functions.

VI. COMMERCIAL RELAY TESTING

Aiming to validate all the protection functions modeled for conducting the tests of this paper, besides using the logic available in manufacturers' commercial relay manuals, practical validation tests were also performed with commercial relays. To perform the practical tests, the COMTRADE files were generated in the PSCAD software and reproduced in the commercial relays using a test case, as illustrated in Fig. 12.

To exemplify the practical tests carried out, Fig. 13 shows the response of the memory-polarized distance function of a
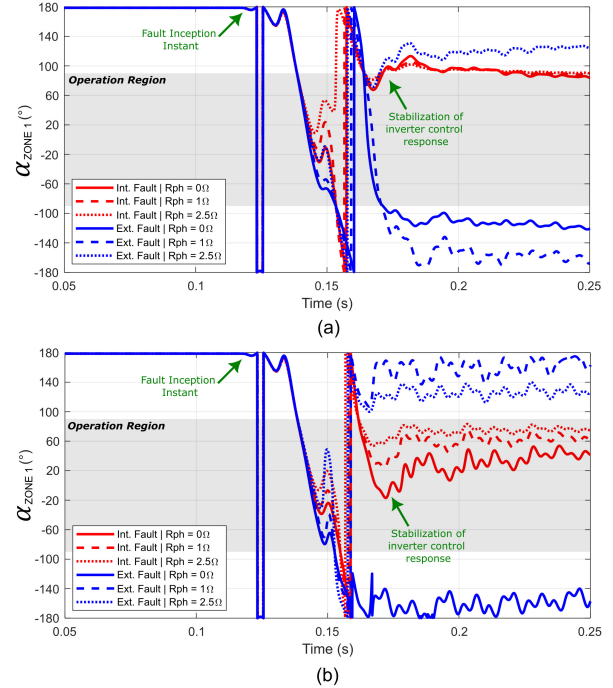
commercial relay, for a bolted AB fault scenario, applied to 50% of Line 1-2 and considering both G1C and G2C. This function was chosen for this demonstration, as it is among the most widely used functions in line protection relays. For the test, the measurements from point P1 (wind power plant side) were considered and the settings adopted for the analyses of Topic V were maintained, i.e., a protection zone covering 75% of the TL impedance and a time delay of 50 ms.
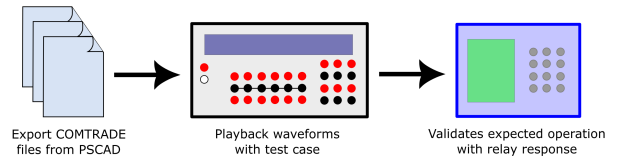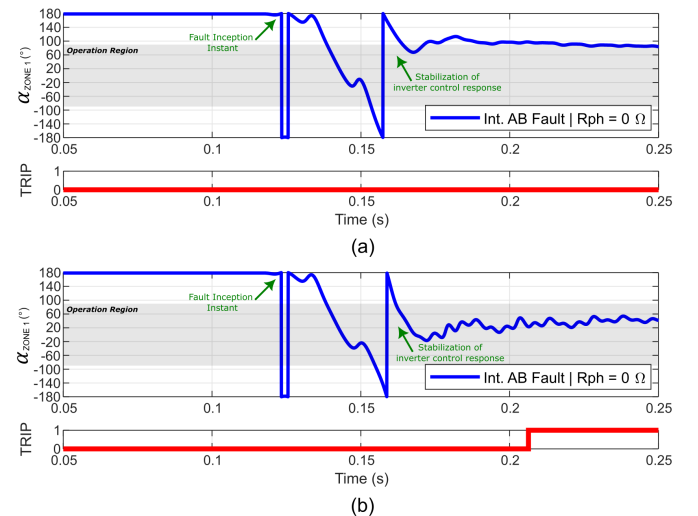

Fig. 12. Testing Set.

Fig. 13. Commercial Relay Testing: obtained results for AB faults at 50% of Line 1-2 considering (a) G1C and (b) G2C.

According to Fig. 13 (a), considering the G1C firstly, it is observed that there was no operation of the distance function for the evaluated time since the phase comparator reaches the operation region about 100 ms after the fault inception instant (disregarding the stabilization time of the inverter control response). When considering the G2C, Fig. 13 (b), it can be observed that the phase comparator reaches the operation region (about 40 ms after the fault incidence), and the function operates after the function time delay since the comparator remains in the operation region. As mentioned in the discussions related to Fig. 11, this is one of the expected behaviors as a benefit of employing the requirements of the IEEE 2800-2022 standard in IBR controls.

VII. Conclusions

This paper presented an EMT-based study about the IEEE 2800-2022 standard benefits for seven transmission line protection functionalities in the presence of IBRs. A total of 8320 fault scenarios were evaluated using the PSCAD software and also employing practical tests with commercial relays. The main findings include the following:

- The quantitative performance studies of the directional protections show that the negative sequence-based functions were significantly benefited by the requirements of IEEE 2800-2022, while the zero sequence-based functions continued to operate satisfactorily;
- For the incremental phasor-based phase-selection function, the benefits of IEEE 2800-2022 were evidenced by a significant increase in the success rate of this function, especially for asymmetrical faults;
- Concerning the current angle-based phase-selection function, the negative sequence injection required by IEEE 2800 proved essential for a good performance;
- Regarding the distance protections, it was observed little influence of the adopted controls for the single-phase fault scenarios. However, for the other fault types, the adoption of IEEE 2800-2022 requirements proved to be indispensable to enhance the protection safety (reduction of undue trips), in addition to a significant increase in the percentage of correct operations. The memory-polarized functions were the most benefited.

References

[1] P. Piya, M. Ebrahimi, M. Karimi-Ghartemani, and S. A. Khajehoddin, "Fault ride-through capability of voltage-controlled inverters," *IEEE Trans. on Industrial Electronics*, vol. 65, no. 10, pp. 7933–7943, 2018.

[2] B. Kasztenny, "Distance elements for line protection applications near unconventional sources," 06 2021.

[3] J. S. Costa *et al.*, "Phasor-based and time-domain transmission line protection considering wind power integration," in *15th Intern. Conf. on Develop. in Power System Protection (DPSP 2020)*, 2020.

[4] Y. Feng, Z. Zhang, Q. Lai, X. Yin, and H. Liu, "Impact of inverter interfaced generators on distance protection," in *2019 4th Intern. Conf. on Intellig. Green Building and Smart Grid*, 2019.

[5] A. Banaiemoqadam, A. Hooshyar, and M. A. Azzouz, "A control-based solution for distance protection of lines connected to converter-interfaced sources during asymmetrical faults," *IEEE Transactions on Power Delivery*, vol. 35, no. 3, pp. 1455–1466, 2020.

[6] K. Jia, Z. Yang, Y. Fang, T. Bi, and M. Sumner, "Influence of inverter-interfaced renewable energy generators on directional relay and an improved scheme," *IEEE Trans. on Power Electronics*, vol. 34, pp. 11 843–11 855, 2019.

[7] A. Haddadi, I. Kocar, and E. Farantatos, "Impact of inverter-based resources on protection schemes based on negative-sequence components," *Technical Brief – Bulk Power System Integration of Variable Generation*, 2019.

[8] A. Hooshyar, E. F. El-Saadany, and M. Sanaye-Pasand, "Fault type classification in microgrids including photovoltaic dgs," *IEEE Tr. on Smart Grid*, pp. 2218–2229, 2016.

[9] M. A. Azzouz, A. Hooshyar, and E. F. El-Saadany, "Resilience enhancement of microgrids with inverter-interfaced dgs by enabling faulty phase selection," *IEEE Transactions on Smart Grid*, vol. 9, pp. 6578–6589, 2018.

[10] J. Chavez, M. Popov, D. López, S. Azizi, and V. Terzija, "S-transform based fault detection algorithm for enhancing distance protection performance," *International Journal of Electrical Power and Energy Systems*, vol. 130, 02 2021.

[11] M. Popov, J. Chavez, E. M. Carrasco, M. T. V. Martínez, S. B. Vicente, D. López, S. Azizi, and V. Terzija, "Enhancing distance protection performance in transmission systems with renewable energy utilization," in *2020 IEEE PES Innovative Smart Grid Technologies Europe (ISGT-Europe)*, 2020, pp. 181–185.

[12] A. Novikov, J. J. de Chavez, and M. Popov, "Performance assessment of distance protection in systems with high penetration of pvs," in *2019 IEEE Milan PowerTech*, 2019, pp. 1–6.

[13] J. Chavez, M. Popov, A. Novikov, S. Azizi, and V. Terzija, "Protection function assessment of present relays for wind generator applications," in *2019 International Conf. on Power Systems Transients*, 2019, pp. 1–6.

[14] "Ieee standard for interconnection and interoperability of inverter-based resources (ibrs) interconnecting with associated transmission electric power systems," *IEEE Std 2800-2022*, pp. 1–180, 2022.

[15] K. Jones, P. Pourbeik, G. Kobet, A. Berner, N. Fischer, F. Huang, J. Holbach, M. Jensen, J. O'Connor, M. Patel, M. Ropp, J. Wen, T. Yang, R. Bauer, R. Cummings, R. Quint, N. Segal, and M. Osman, "Impact of inverter based generation on bulk power system dynamics and short-circuit performance," 07 2018.

[16] T. Kauffmann *et al.*, "Short-circuit model for type-iv wind turbine generators with decoupled sequence control," *IEEE Transactions on Power Delivery*, vol. 34, no. 5, pp. 1998–2007, 2019.

[17] U. F. E. R. Commission, "Interconnection for wind energy docket no. rm05-4-001," 2005.

[18] VDE, "Vde ar-n 4120:2018-11. technical requirements for the connection and operation of customer installations to the high voltage network," 2018.

[19] F. V. Lopes, M. J. B. B. Davi, M. Oleskovicz, and G. Fabris, "Importance of emt-type simulations for protection studies in power systems with inverter-based resources," in *IEEE Workshop on Communication Networks and Power Systems (WCNPS)*, 2022, pp. 1–6.

[20] O. Tremblay, R. Gagnon, and M. Fecteau, in *2013 International Conference on Power Systems Transients*.

[21] K. Clark, N. Miller, and J. Sanchez-Gasca, in *General Electric International Inc.*

[22] N. Miller, J. Sanchez-Gasca, W. Price, and R. Delmerico, "Dynamic modeling of ge 1.5 and 3.6 mw wind turbine-generators for stability simulations," in *2003 IEEE Power Engineering Society General Meeting (IEEE Cat. No.03CH37491)*, vol. 3, 2003, pp. 1977–1983 Vol. 3.

[23] E. O. Schweitzer and J. Roberts, "Distance relay element design," *19th Annual West. Prot. Relay Conf.*, 1992.

[24] A. Guzmán, J. Roberts, and D. Hou, "New ground directional elements operate reliably for changing system conditions," *50th Annual Conf. for Prot. Relay Eng.*, 1997.

[25] G. Benmouyal and J. Mahseredjian, "A combined directional and faulted phase selector element based on incremental quantities," *IEEE Transactions on Power Delivery*, vol. 16, pp. 478–484, 2001.

[26] A. Guzmán, M. V. Mynam, V. Skendzic, and J. L. Eternod, "Directional elements - how fast can they be?" *44th Annual Western Protective Relay Conference*, 2017.

[27] D. Costello and K. Zimmerman, "Determining the faulted phase," *63rd Annual Conference for Protective Relay Engineers*, pp. 1–20, 2010.

[28] B. Kasztenny, "Phase selection for single-pole tripping – weak infeed conditions and cross-country faults," 10 2000.

[29] G. Ziegler, *Numerical Distance Protection: Principles and Applications, 4th Ed.* Erlangen: Germany: Publicis Publishing, 2011.

[30] K. Silva and M. Almeida, "Positive sequence voltage memory filter for numerical digital relaying applications," *Electronics Letters*, vol. 51, no. 21, pp. 1697–1699, 2015.